Fluid Dynamics &
Materials Processing

Tech Science Press

http://doi.org/10.32604/fdmp.2026.075360

ARTICLE

Multiscale Single-Phase Flow Mechanisms of Shale Oil Revealed by High-Pressure Nuclear Magnetic Resonance Experiments

Maolei Cui[1,2,*], Zengmin Lun[1,2], Jie Zhang[1,2], Jun Niu[1,2] and Pufu Xiao[1,2]

[1]State Key Laboratory of Shale Oil and Gas Enrichment Mechanisms and Effective Development, Beijing, China
[2]Petroleum Exploration and Production Research Institute, SINOPEC, Beijing, China
*Corresponding Author: Maolei Cui. Email: cuiml.syky@sinopec.com

Received: 30 October 2025; Accepted: 13 February 2026; Published: 04 March 2026

ABSTRACT: To clarify fluid flow mechanisms and establish effective development conditions in continental shale oil reservoirs, a high-temperature, high-pressure steady-state flow system integrated with nuclear magnetic resonance (NMR) technology has been developed. The apparatus combines sample evacuation, rapid pressurization and saturation, and controlled displacement, enabling systematic investigation of single-phase shale oil flow under representative reservoir conditions. Related experiments allow proper quantification of the activation thresholds and relative contributions of different pore types to flow. A movable fluid index (MFI), defined using dual T_2 cutoff values, is introduced accordingly and linked to key flow parameters. The results reveal distinct multi-scale characteristics of single-phase shale oil transport, namely micro-scale graded displacement and macro-scale segmented nonlinear behavior. As the injection–production pressure difference increases, flow pathways are activated progressively, beginning with fractures, followed by large and then smaller macropores, leading to a pronounced enhancement in apparent permeability. Although mesopores and micropores contribute little to direct flow, their indirect influence becomes increasingly important, and apparent permeability gradually approaches a stable limit at higher pressure difference. It is also shown that the MFI exhibits a strong negative correlation with the starting pressure gradient and a positive correlation with apparent permeability, providing a rapid and reliable indicator of shale oil flow capacity. Samples containing through-going fractures display consistently higher MFI values and superior flowability compared with those dominated by laminated fractures, highlighting the pivotal role of well-connected fracture networks generated by large-scale hydraulic fracturing in improving shale oil production.

KEYWORDS: Shale oil; laminated fractures; steady-state flow; Nuclear Magnetic Resonance (NMR); nonlinear flow

1 Introduction

Shale oil is hosted in organic-rich shale formations, typically lacks natural productivity or fails to meet industrial production thresholds, thus requiring necessitating hydraulic fracturing for commercial exploitation. Consequently, the exploration and development shale oil have become a strategic priority in China's oil and gas industry [1–3]. In recent years, substantial shale oil resources have been discovered in multiple basins, including the Jiyang Depression in the Shengli area, the Subei Basin, the Sichuan Basin, and the Ordos Basin [4–7], demonstrating enormous development potential. However, research on the mechanisms of shale oil extraction lags significantly behind field production practices, particularly regarding the flow capacity of shale oil [8,9].

Shale reservoirs are characterized by widespread micro-nanopore structures where fluid flow is governed by multiple factors, such as starting pressure gradients, capillary pressure, and pore

connectivity [10–13]. These complexities render traditional flow theories and core flow experimental methods inadequate for accurately characterizing the flow properties of shale oil. Recent advances have deepened the understanding of relevant mechanisms: a study on continental shale reservoirs highlighted that low-velocity nonlinear flow is dominated by fluid-solid interface slip effects and adsorption boundary layer effects, with pore-fracture combination modes significantly affecting apparent permeability [14]; molecular dynamics simulations of 26-component oil in real shale kerogen and quartz nanopores revealed flow regime transitions with pressure gradients-from parabolic to piston-like velocity profiles-which directly impact flow efficiency [15]. Notably, nuclear magnetic resonance (NMR) technology has emerged as a powerful tool for probing shale fluid behavior, though most research has focused on marine shale; comparative studies show that continental shale exhibits distinct imbibition characteristics due to its higher clay mineral content, with T_2 values decreasing during water imbibition (a result of matrix pore destruction) that negatively affects flow channels [16]. Despite these advancements, the integration of NMR with high-temperature, high-pressure steady-state flow experiments to quantify movable fluid and pore activation in continental shale oil remains insufficiently explored [17,18].

To address the challenges of low oil saturation and the unique steady-state flow characteristics of continental shale oil reservoirs, the innovative non-magnetic high-temperature and high-pressure steady-state flow experimental apparatus was developed. By precisely controlling confining pressure and pore pressure, the apparatus integrated sample-evacuation, rapid pressure saturation, and displacement. NMR technology is employed to dynamically monitor the microscopic distribution of fluids during displacement, addressing the gap in tailored NMR applications for continental shale [19]. Single-phase flow experiments were conducted on investigate the flow characteristics of shale oil under different pressure gradients and to clarify new insights into the nonlinear flow mechanisms. This work aims to enhance the understanding of fluid transport and recovery in unconventional reservoirs, providing theoretical support for optimizing fracturing techniques and improving recovery efficiency.

2 Experiments

2.1 Experimental Samples

The experimental samples were used without cleaning and classified into two categories based on their fracture characteristics and lithology. Sample 41# is a laminated and stratified calcareous mudstone containing laminated fractures. Sample 196A#, 120# and 82# are blocky and stratified calcareous mudstone containing through-going fractures. The experimental samples are shown in Fig. 1.

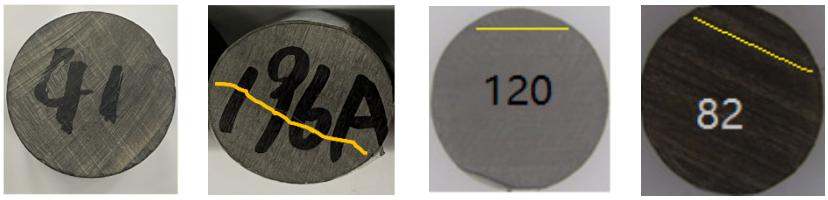

(**a**) (**b**) (**c**) (**d**)

Figure 1: Experimental samples. (**a**) Laminated and stratified calcareous mudstone (with laminated fractures); (**b**–**d**) Blocky and stratified calcareous mudstone (with through-going fractures).

The porosity and permeability of the shale samples were measured using the helium porosimetry method and the pulse decay method. Due to the presence of fractures in the samples to varying degrees, their gas permeability values exceeded the 10^{-1} mD range. The sample containing laminated fractures

exhibited relatively lower permeability compared to the other. The basic physical properties of the samples are summarized in Table 1.

Table 1: Basic parameters of samples.

No.	Length (cm)	Diameter (cm)	K (10^{-3} mD)	φ (%)
41#	2.563	2.498	0.332	6.21
196A#	2.407	2.446	1.371	1.16
120	2.431	2.507	1.583	2.26
82	2.550	2.495	2.162	6.56

2.2 Experimental Fluids

Experiments were conducted using n-dodecane and fluorocarbon oil (which generates no NMR signal) as the experimental fluids, under conditions of 50°C and 7.5 MPa.

2.3 Experimental Device

The experimental workflow is shown in Fig. 2. The apparatus consists of the following key components:

(1) NMR System: Comprises an NMR control system, permanent magnet, probe, and imaging software. The system operates at a magnetic field strength of 0.047 T with a uniformity better than 100 ppm, a proton resonance frequency of 2.0 MHz, a maximum operating temperature of 60°C, and a minimum echo time of 60 μs.

(2) High-Pressure High-Precision Displacement System: Consists of two high-precision Vindum dual-cylinder plunger pumps (imported from the USA). Each pump can achieve a maximum pressure of 82.7 MPa, a minimum flow rate of 0.00001 mL/min, and a pressure control precision of 1.38×10^{-2} MPa. One pump controls the confining pressure, while the other regulates the pore pressure during displacement.

(3) Intelligent Non-Magnetic Core Holder: Enable integrated experimental steps-evacuation, rapid pressurization, saturation, and displacement—through precise and independent control of confining and pore pressures. The displacement pump raises the pore pressure inside the sample, and the confining-pressure pump pressurizes the annular space surrounding the sample. Schematic diagram of the intelligent core holder is shown in Fig. 3.

Rapid Pressurization and Oil Saturation:

When the confining pressure is lower than the pore pressure, the sample sleeve expands outward due to the pressure difference. This expansion activates the saturation sealing ring, which isolates the pore and confining pressure zones while deactivating the displacement sealing ring. High-pressure fluid can then contact the entire outer surface of the sample, enabling rapid pressurization and oil saturation. Saturation is complete once the displacement pump stops injecting fluid into the sample.

Fluid Flow Simulation:

When the confining pressure is at least 3 MPa higher than the pore pressure, the sleeve compresses inward. This activates the displacement sealing ring, such that injected fluid can enter the sample only through its end face. This configuration allows for controlled simulation of internal fluid flow.

The innovative design ensures precise experimental control, enables seamless transitions between different experimental stages, and significantly improves the efficiency and accuracy of shale-oil flow studies.

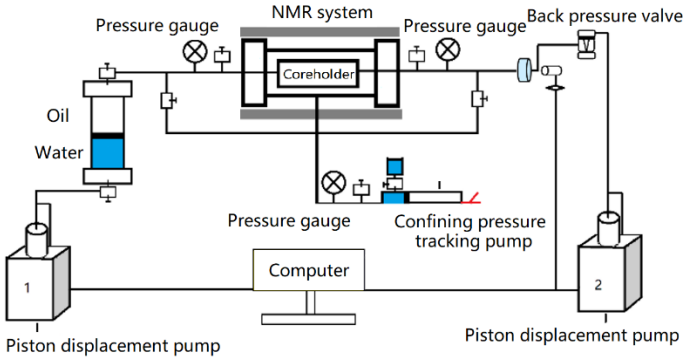

Figure 2: Experimental workflow of high-temperature high-pressure steady-state flow of shale oil.

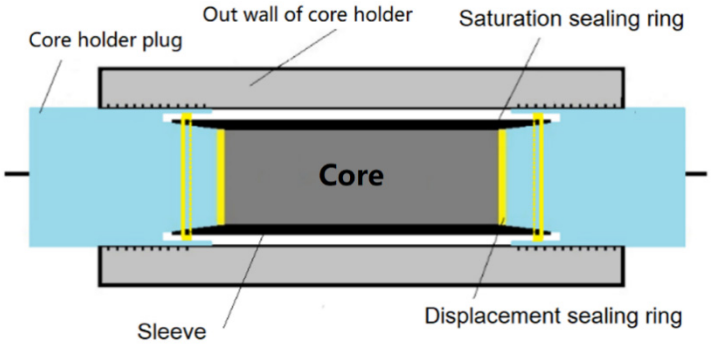

Figure 3: Schematic diagram of the intelligent core holder.

2.4 Experimental Procedure

(1) Sample Evacuation and Saturation

The shale core was placed in the core holder and evacuated using a molecular vacuum pump (vacuum down to 10^{-5} mbar) for 72 h. N-dodecane was injected at different pressures, with each pressure point equilibrated for more than 6 h to fully saturate the sample. Continuous monitoring and recording of the NMR T_2 spectra were performed until the T_2 spectra curve showed no further changes, indicating that the core was fully saturated. The final T_2 spectra represented the initial T_2 curve of the saturated oil in the sample.

(2) Single-phase flow experiment

The injected fluid was replaced with fluorocarbon oil, which has a similar viscosity to n-dodecane. The pressure difference was established by decreasing the outlet pressure of the sample to inject fluorocarbon oil for displace n-dodecane. The single-phase oil flow experiment was conducted until a stable flow rate was achieved. The NMR T_2 spectra were recorded after the flow stabilized.

(3) Single-phase flow experiment at different pressure difference

Steps (1) and (2) were repeated, adjusting the sample outlet pressure to establish different pressure difference, and the steady-state flow rates corresponding to each difference were measured.

(4) Flow rate vs. pressure difference curve

The relationship between flow rate and pressure difference was plotted.

3 Result and Discussion

3.1 Differentiated Movable Oil Characteristics in Shale

The initial NMR signal of fresh samples reflected the amount of immovable fluids within the sample, including hydrogen-containing substances such as kerogen and bound oil/water. After vacuum saturation, the cumulative NMR signal represented the volume of oil entering the sample, indicating the movable oil content.

For the sample 41#, oil saturation experiments were conducted under pressure of 0.1 MPa, 0.2 MPa, 0.5 MPa, and 1.0 MPa. Fig. 4 illustrates the relationship between the cumulative NMR signal and saturation pressure gradient. The results show that as the pressure gradient increased, the movable oil volume increased linearly. However, after 0.2 MPa, the growth rate slowed, forming a noticeable inflection point.

The segment before the inflection point represents low-pressure-gradient movable oil, while the segment after represents high-pressure-gradient movable oil, which has higher flow resistance and is more difficult to mobilize. Fig. 5 shows the relationship between NMR signal amplitude and T_2 relaxation time under different saturation pressure gradients.

Using T_2 cut-off values to distinguish movable from immovable fluids, and further dividing movable oil into low-pressure and high-pressure types, two cut-off values, T_2 and T_2' were defined. The greater the difference between T_2' and T_2, the higher the proportion of low-pressure-gradient movable oil, and the stronger the shale oil flowability.

The Movable Fluid Index (MFI), defined as the ratio of T_2' to T_2, was introduced to quantify this effect. A higher MFI indicates a greater proportion of low-pressure-gradient movable oil and stronger shale oil flowability. The physical meaning of MFI is a normalized, dimensionless key parameter used to quantify and compare the ease of oil flow and the production potential across different shale reservoirs. It can transform static information (fluid distribution) into a dynamic indicator of development potential.

$$MFI = T_2'/T_2 \tag{1}$$

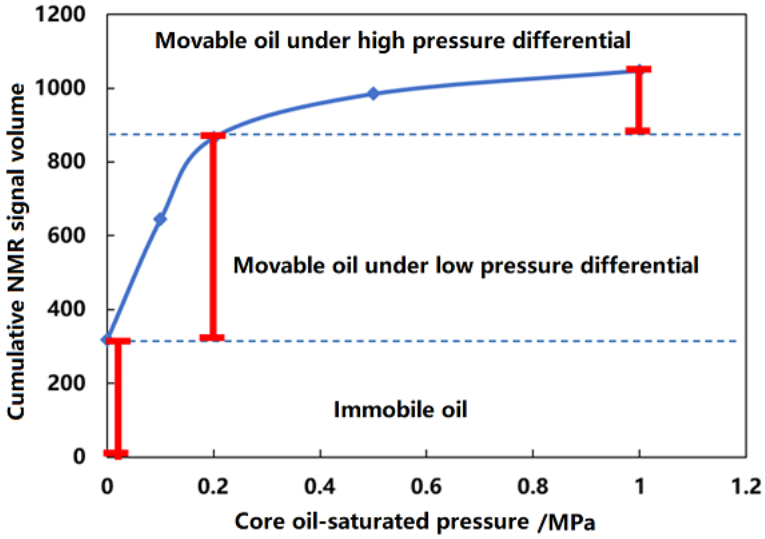

Figure 4: Relationship between cumulative NMR signal and saturation pressure gradient.

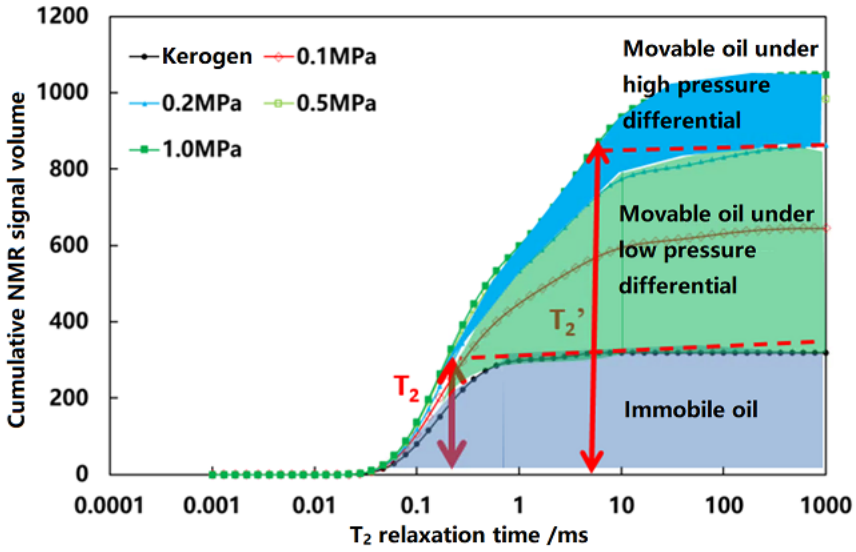

Figure 5: NMR spectra for different pressure gradients.

3.2 Micro-Scale Gradual Sweep and Flow Characteristics

For the sample 41#, fluorinated oil was used to displace n-dodecane under different pressure gradients. Changes in NMR signals from various pore types reflected the ease and extent of pore participation in flow. Faster and larger signal changes indicated higher flow capacity and greater pore participation.

Li et al. proposed a NMR method for investigating the pore structure of tight sandstone [20]. Combined with mercury intrusion experiments, the proportions of different pore types were analyzed (Figs. 6 and 7). Pore types were classified according to the IUPAC standards [21] as follows:

- Micropores (pores radius $\leq$ 0.002 μm)
- Mesopores (pores radius between 0.002 and 0.05 μm)
- Smaller macropores (pores radius between 0.05 and 1 μm)
- Larger macropores (pores radius $\geq$ 1 μm, including laminar fractures)

Fig. 6 depicts the variation curves of crude oil signal intensity in different types of pores with respect to pressure difference. In the experiment, NMR-silent crude oil was used to displace the NMR-active crude oil originally present in the pores. A greater decline amplitude of the curve corresponds to a larger volume of mobile crude oil participating in the flow within the pores. Thus, these curves can effectively characterize the producibility of crude oil in various pore types under different pressure difference conditions. As shown in Fig. 6, under the initial conditions, the sample contains a higher number of mesopores and smaller macropores (with the quantity proportional to the signal intensity), followed by larger macropores, while micropores and fractures are relatively scarce. As the pressure difference across the sample increases, the NMR signal intensity of different pore types gradually decreases, but the rate and extent of this decrease vary significantly. Fractures and larger macropores are the first to participate in fluid flow, with the number of such pores involved in flow increasing over time. Smaller macropores follow, with a noticeable increase in the number of participating pores under larger pressure difference (indicated by a downward trend at the end of the orange curve). Flow in mesopores and micropores is not significant, though weak fluid exchange is observed (indicated by slight fluctuations in the curve). Fig. 7 depicts the variation curves of the proportion of crude oil signal intensity in different types of pores with respect to pressure difference. These curves illustrate the contribution rate of the produced crude oil from various pore types to the total production

during the displacement process-higher curve values indicate a greater contribution of the corresponding pore type to oil production. As shown in Fig. 7, with increasing pressure difference, the proportion of different pore types involved in flow varies significantly. The primary contributors to flow are smaller macropores and larger macropores, each accounting for nearly 49% (with their combined contribution nearing 98%). Due to their large quantity, the weak fluid exchange in mesopores exerts a considerable impact on flow, which increases significantly with pressure difference. Micropores and fractures, being less abundant, contribute minimally to the overall flow. This analysis indicates that the micro-scale flow of shale oil exhibits hierarchical, cascading behavior, which significantly influences the macroscopic flow characteristics of the sample.

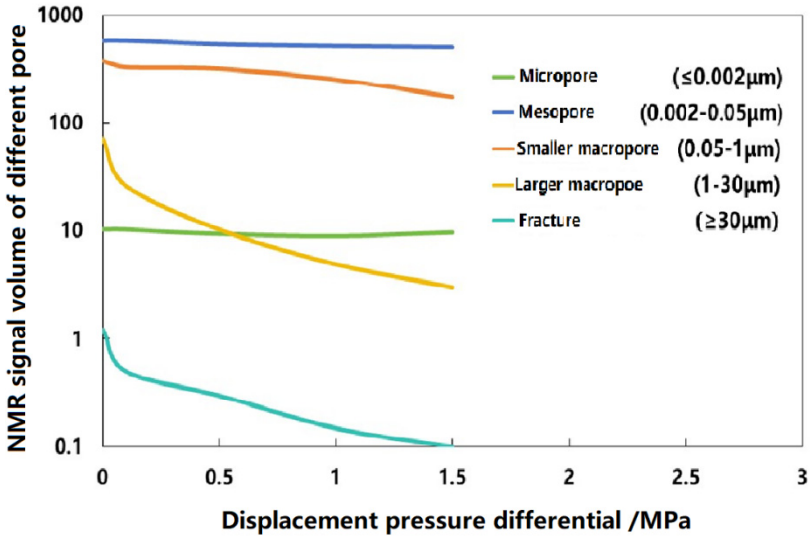

Figure 6: Changes in NMR signals from different pore types during displacement.

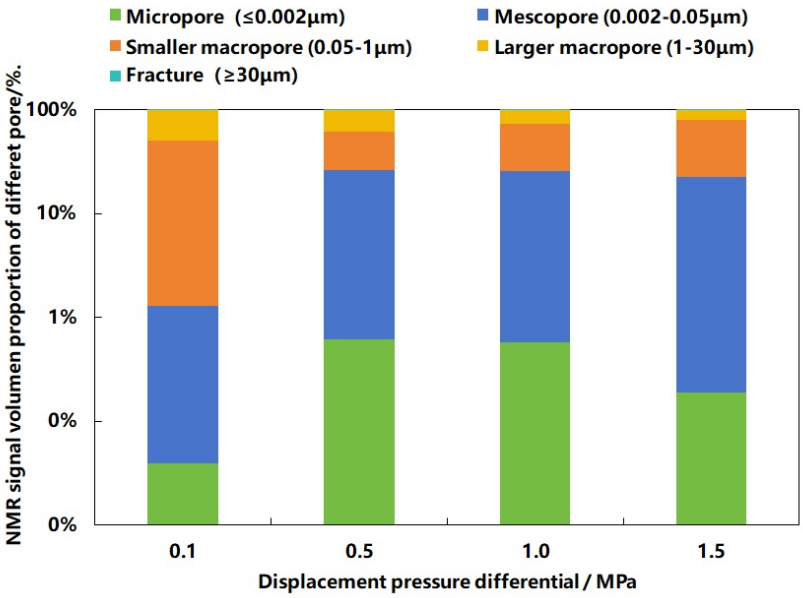

Figure 7: Proportions of different pore types participating in flow.

3.3 Segmented Nonlinear Flow Characteristics in Shale Oil

Through single-phase steady-state oil flow experiments on shale samples, the relationships between flow rate, apparent permeability, and pressure difference were obtained (Figs. 8 and 9). The results indicate that both flow rate and apparent permeability exhibit distinct segmented characteristics with increasing pressure difference. The flow rate initially increases slowly and then transitions to a rapid rise: When the pressure difference is below 0.2 MPa, the relationship between flow rate and pressure difference is nonlinear. When the pressure difference exceeds 0.2 MPa, the relationship becomes approximately linear. Apparent permeability shows a rapid initial increase followed by a gradually stabilization.

Based on the observed microscopic hierarchical flow behavior, an increasing pressure difference leads to the continuous expansion of the microscopic flow range, which influences the flow process in two significant ways. Firstly, the number of smaller and larger macropores preferentially participating in flow increases, leading to a gradual rise in flow rate and apparent permeability. Secondly, as the pressure difference increases, mesopores with higher flow resistance are activated, and their participation in flow increases. This causes a rapid rise in flow rate, though the rate of increase is smaller than that of the pressure difference, resulting in a deceleration in permeability growth that eventually stabilizes.

Quadratic regression analysis was performed on the flow rate versus pressure difference curve to determine its intersection with the x-axis, which represents the start-up pressure gradient. Apparent permeability was calculated using Darcy's law, and the start-up pressure gradient and apparent permeability are summarized in Table 2. Compared to Sample #41, Sample #196 (containing through-going fractures) exhibits a start-up pressure gradient nearly four times lower and an apparent permeability more than twice as high. This finding further demonstrates that through-going fractures induced by hydraulic fracturing can effectively reduce the start-up pressure gradient of the shale matrix, expand the effective mobilization range, and significantly enhance the overall seepage capacity of shale reservoirs.

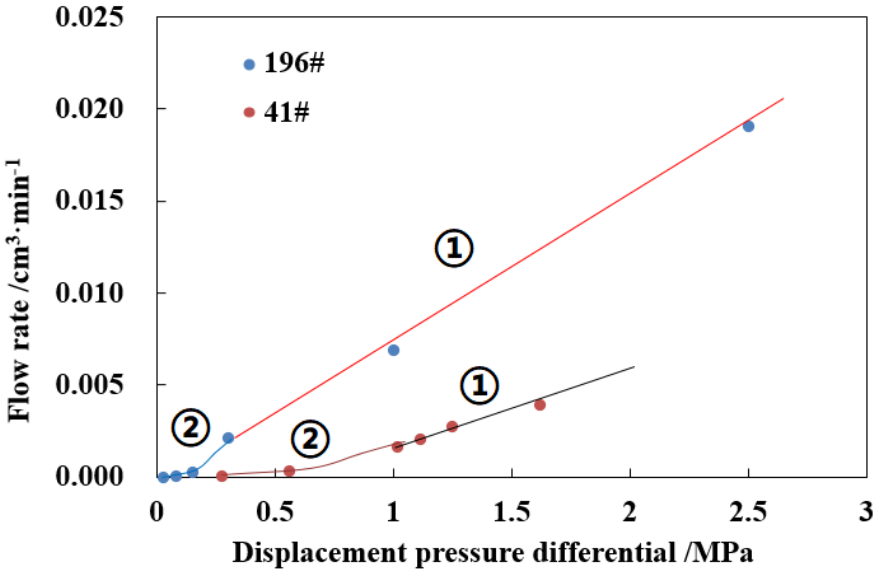

Figure 8: The relationships between flow rate and displacement pressure difference.

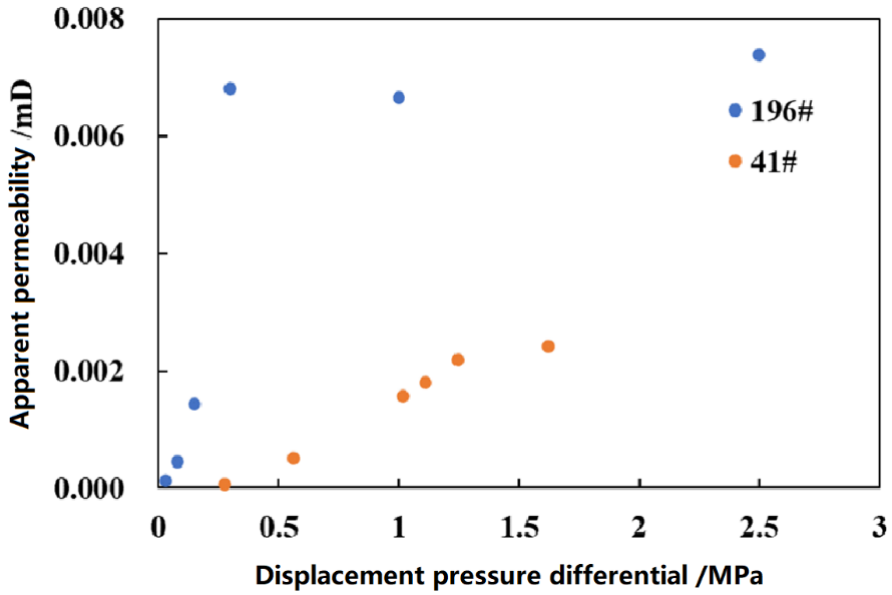

Figure 9: The relationships between apparent permeability and displacement pressure difference.

As shown in Table 2 and Fig. 10, the movable fluid index demonstrates a strong correlation with the start-up pressure gradient and apparent permeability. A larger movable fluid index corresponds to a lower start-up pressure gradient, higher apparent permeability, and stronger shale oil flow capacity. A functional relationship has been established between MFI, threshold pressure gradient and apparent permeability: specifically, threshold pressure gradient exhibits a power-law relationship with MFI, while apparent permeability shows a logarithmic relationship with MFI. Therefore, the method of sample evacuation and pressurized oil saturation can be effectively used to rapidly evaluate the single-phase flow capacity of shale oil, providing a new theoretical parameter for assessing shale oil flow capability.

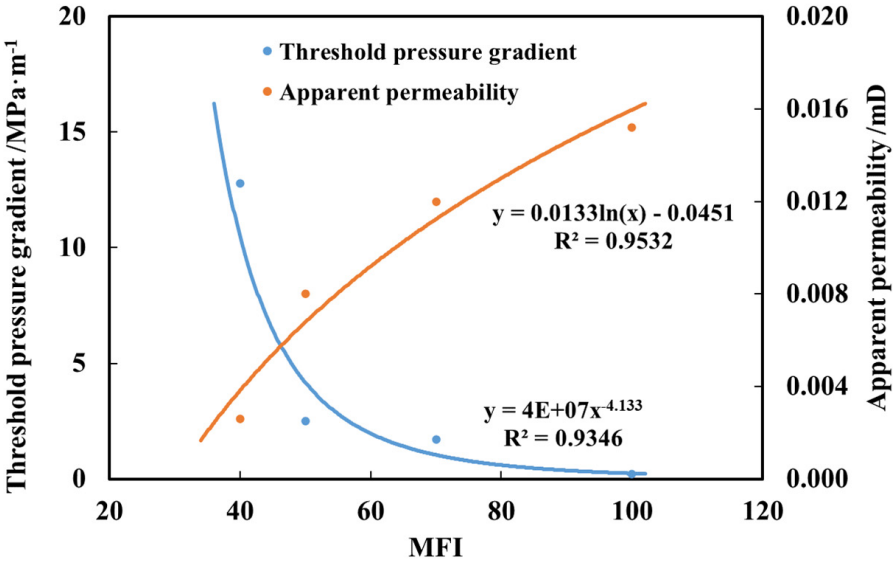

Figure 10: The relationships between MFI and apparent permeability/threshold pressure gradient.

Table 2: Results of single-phase steady-state oil flow experiment.

Sample No.	Lithology	MFI	Threshold Pressure Gradient /MPa·m^{-1}	Apparent Permeability /mD
41#	Laminated and lamellar calcareous mudstone (with lamellar fractures)	40.3	12.8	0.0026
196#	Massive-laminated calcareous mudstone (with through-going fractures)	51.1	2.5	0.0080
120#	Massive-laminated calcareous mudstone (with through-going fractures)	70.5	1.7	0.0120
82#	Massive-laminated calcareous mudstone (with through-going fractures)	98.2	0.2	0.0152

4 Conclusions

(1) Movable Fluid Index Based on Dual T_2 Cutoff Values

Based on the evolution of NMR T_2 spectra during core evacuation and pressurized oil saturation, a movable fluid index (MFI) defined by dual T_2 cutoff values is proposed. This index classifies shale fluids into three categories: immobile fluid, low-pressure movable oil, and high-pressure movable oil. A higher MFI corresponds to a greater proportion of low-pressure movable oil, a lower start-up pressure gradient, and a higher apparent permeability. Thus, the MFI can serve as a key parameter for the rapid assessment of shale-oil flow capacity.

(2) Hierarchical Cascading Flow at Micro- and Macroscopic Scales

Shale-oil flow is characterized by hierarchical cascading behavior at the microscopic scale and segmented nonlinear behavior at the macroscopic scale. As the pressure difference increases, flow initiates in fractures, followed by larger macropores, and then smaller macropores, with each contributing progressively to the overall flow. Although mesopores and micropores contribute little individually, the collective effect of abundant mesopores is non-negligible. Macroscopically, apparent permeability rises rapidly at low pressure difference and then plateaus.

(3) Impact of Fracture Type on Flow Performance

Compared to samples with laminated fractures, those containing through-going fractures exhibit a significantly lower start-up pressure gradient. This indicates that a complex fracture network generated by large-scale volume fracturing can effectively reduce the start-up pressure gradient, expand the range of pore-scale flow pathways, and enhance the apparent permeability of the shale reservoir.

Acknowledgement: The authors would like to thank Shengli Oilfield for providing the shale samples to support this study.

Funding Statement: This work is mainly supported by the National Science and Technology Major Project of China (Grant No. 2024ZD 1004302) and the Key Scientific and Technological Research project of SINOPEC (Grant No. P25186).

Author Contributions: The authors confirm contribution to the paper as follows: Conceptualization, Maolei Cui; methodology, Maolei Cui and Zengmin Lun; validation, Jie Zhang; formal analysis, Jun Niu; investigation, Maolei Cui; resources, Zengmin Lun; data curation, Pufu Xiao; writing—original draft preparation, Maolei Cui; writing—review and editing, Maolei Cui; visualization, Pufu Xiao; supervision, Jie Zhang; project administration, Jun Niu;. All authors reviewed and approved the final version of the manuscript.

Availability of Data and Materials: The data that support the findings of this study are available from the Corresponding Author, upon reasonable request.

Ethics Approval: Not applicable.

Conflicts of Interest: The authors declare no conflicts of interest.

References

1. Guo XS, Ma XX, Li MW, Li ZM, Qin H, Wang Y, et al. Discussion on the enrichment mechanism of continental shale oil. Oil Gas Geol. 2023;44(6):1333–49. [CrossRef].
2. Li Z, Liu J, Su Y, Fan L, Hao Y, Kanjibayi B, et al. Influences of diffusion and advection on dynamic oil-CO_2 mixing during CO_2 EOR and storage process: Experimental study and numerical modeling at pore-scales. Energy. 2023;267:126567. [CrossRef].
3. Ma YS, Cai XY, Zhao PR. Theoretical understanding and practice of shale gas exploration and development in China. Pet Explor Dev. 2018;45(4):561–74. [CrossRef].
4. Li Z, Su Y, Shen F, Huang L, Ren S, Hao Y, et al. Investigation of CO_2 storage and EOR of alternating N_2 and CO_2 injection using experiments and numerical simulation. Fuel. 2023;340:127517. [CrossRef].
5. Li Z, Lei Z, Shen W, Martyushev DA, Hu X. A comprehensive review of the oil flow mechanism and numerical simulations in shale oil reservoirs. Energies. 2023;16(8):3516. [CrossRef].
6. Tian Y, Qu Z, Wang P, Liu N, Ju B, Zhan J, et al. Effect of wettability and CO_2 on asphaltene precipitation in shale oil reservoir. Energy Fuels. 2023;37(20):15744–52. [CrossRef].
7. Xu S, Gou Q. The importance of laminae for China lacustrine shale oil enrichment: A review. Energies. 2023;16(4):1661. [CrossRef].
8. Dai C, Cheng R, Sun X, Liu Y, Zhou H, Wu Y, et al. Oil migration in nanometer to micrometer sized pores of tight oil sandstone during dynamic surfactant imbibition with online NMR. Fuel. 2019;245:544–53. [CrossRef].
9. Huang X, Tian Z, Zuo X, Li X, Yang W, Lu J. The microscopic pore crude oil production characteristics and influencing factors by DME-assisted CO_2 injection in shale oil reservoirs. Fuel. 2023;331:125843. [CrossRef].
10. Ibrahim AF, Elkatatny S. Data-driven models to predict shale wettability for CO_2 sequestration applications. Sci Rep. 2023;13:10151. [CrossRef].
11. Na JG, Im CH, Chung SH, Lee KB. Effect of oil shale retorting temperature on shale oil yield and properties. Fuel. 2012;95:131–5. [CrossRef].
12. Wang X, Zhang G, Tang W, Wang D, Wang K, Liu J, et al. A review of commercial development of continental shale oil in China. Energy Geosci. 2022;3(3):282–9. [CrossRef].
13. Xu Y, Lun Z, Pan Z, Wang H, Zhou X, Zhao C, et al. Occurrence space and state of shale oil: A review. J Petrol Sci Eng. 2022;211:110183. [CrossRef].
14. Zhang Y, Wang XG, Li H, Liu YW, Sun FJ, Yang SL. Nonlinear flow mechanisms of continental shale oil considering interface slip effects. J Nat Gas Sci Eng. 2025;132:106789. [CrossRef].
15. Li Z, Wang X, Kou J, Sun H, Li Y, Zheng L, et al. Flow regime transition of multicomponent oil in shale nanopores. Fuel. 2024;359:130431. [CrossRef].
16. Yang L, Dou N, Lu X, Zhang X, Chen X, Gao J, et al. Advances in understanding imbibition characteristics of shale using an NMR technique: A comparative study of marine and continental shale. J Geophys Eng. 2018;15(4):1363–75. [CrossRef].
17. Cui ML, Lun ZM, Zhang J, Lang DJ, Zhang H, Zhao CP, et al. Experimental study on shale oil flow characteristics under high-temperature and high-pressure conditions. Pet Explor Dev. 2024;51(3):589–98. [CrossRef].
18. Lu Y, Liu Y, Tang J, Jia Y, Tian R, Zhou J, et al. Water wettability alternation of CO_2-water-shale system due to nanoparticles: Implications for CO_2 geo-storage. Int J Greenh Gas Control. 2023;124:103836. [CrossRef].
19. Wang FY, Yue H, Zhu WY. Apparent permeability model of shale oil reservoirs considering nano-confinement effects and pore-fracture combination modes. Acta Pet Sin. 2025;46(4):779–88. [CrossRef].

20. Li HB, Zhu JY, Guo HK. Study on pore radius distribution converted by nuclear magnetic resonance T2 spectrum. J Spectrosc. 2008;25(2):273–80. [CrossRef].

21. Ali F, Negash BM, Ridha S, Abdulelah H. A review on the interfacial properties of caprock/CO_2/brine system-implications for structural integrity of deep saline aquifers during geological carbon storage. Earth Sci Rev. 2023;247:104600. [CrossRef].